scientific data



DATA DESCRIPTOR

OPEN AMD-SD: An Optical Coherence **Tomography Image Dataset for** wet AMD Lesions Segmentation

Yunwei Hu^{1,3}, Yundi Gao^{1,3}, Weihao Gao^{2,3}, Wenbin Luo¹, Zhongyi Yang¹, Fen Xiong¹, Zidan Chen¹, Yucai Lin¹, Xinjing Xia¹, Xiaolong Yin¹⊠, Yan Deng¹⊠, Lan Ma²⊠ & Guodong Li¹⊠

Wet Age-related Macular Degeneration (wet AMD) is a common ophthalmic disease that significantly impacts patients' vision. Optical coherence tomography (OCT) examination has been widely utilized for diagnosing, treating, and monitoring wet AMD due to its cost-effectiveness, non-invasiveness, and repeatability, positioning it as the most valuable tool for diagnosis and tracking. OCT can provide clear visualization of retinal layers and precise segmentation of lesion areas, facilitating the identification and quantitative analysis of abnormalities. However, the lack of high-quality datasets for assessing wet AMD has impeded the advancement of related algorithms. To address this issue, we have curated a comprehensive wet AMD OCT Segmentation Dataset (AMD-SD), comprising 3049 B-scan images from 138 patients, each annotated with five segmentation labels: subretinal fluid, intraretinal fluid, ellipsoid zone continuity, subretinal hyperreflective material, and pigment epithelial detachment. This dataset presents a valuable opportunity to investigate the accuracy and reliability of various segmentation algorithms for wet AMD, offering essential data support for developing AI-assisted clinical applications targeting wet AMD.

Background & Summary

Age-related macular degeneration (AMD) is one of the main causes of irreversible vision loss in people aged 50 years and older. Globally, an estimated 8.69% of the population aged from 45 to 85 is afflicted with AMD, with projections that by 2040, approximately 288 million individuals worldwide will be affected by the condition 1. AMD is divided into dry AMD (geographic atrophy) and neovascular AMD (also known as wet AMD), both forms of which can precipitate rapid vision loss². Presently, effective treatment modalities for dry AMD are lacking^{3,4}. In contrast, wet AMD is typified by choroidal neovascularization (CNV) or retinal neovascularization, leading to pronounced changes including retinal edema, hemorrhage, exudation, and scarring⁵. Primary treatment for wet AMD entails intravitreal administration of anti-vascular endothelial growth factor (VEGF) agents, which is capable of mitigating or reversing disease progression^{6–12}.

Optical coherence tomography (OCT), a non-invasive, high-resolution imaging modality, offers rapid acquisition of cross-sectional macular images^{13,14}. Its simplicity, speed, and non-invasive nature render OCT a cost-effective, repeatable tool for diagnosing, managing, and monitoring wet AMD. By facilitating visualization of retinal layers and pertinent features of wet AMD, such as subretinal fluid (SRF), intraretinal fluid (IRF), ellipsoid zone continuity, subretinal hyperreflective material (SHRM), and pigment epithelial detachment (PED), OCT enables precise disease assessment, prognostication, and informed clinical decision-making. This personalized approach optimizes treatment outcomes by tailoring regimens to individual responses, thus enhancing patient compliance and alleviating economic burdens. Nevertheless, manual lesion size measurements from OCT B-scans are labor-intensive and susceptible to inter-observer variability, warranting caution in clinical interpretation.

Leveraging artificial intelligence (AI) technology, scholars have predominantly concentrated on establishing OCT-based models for AMD diagnosis and treatment response prediction, including diagnostic models 15,16,

¹Ophthalmic Center, The Second Affiliated Hospital, Jiangxi Medical College, Nanchang University, Nanchang, 330000, P. R. China. ²Shenzhen International Graduate School, Tsinghua University, Lishui Rd, Shenzhen, 518055, Guangdong, P. R. China. ³These authors contributed equally: Yunwei Hu, Yundi Gao, Weihao Gao. [™]e-mail: yinxiaolong22216@163.com; Dengyan789789@hotmail.com; malan@sz.tsinghua.edu.cn; daliquodong@sina.com

Reference	Num. of Images	Disease Task		Segmentation Type	
Chiu et al.37	220	AMD	SEG	RPE, RPE drusen complex, and total retina	
Farsiu et al. ³⁸	38,400	AMD	SEG	RPE, RPE drusen complex, and total retina	
Srinivasan ³⁹	3,231	DME, AMD, H.E.	CLS	_	
Stephanie et al.40	610	DME	SEG	Fluid, Structure Layers	
Rashno et al.41	600	AMD	SEG	IRF, SRF	
Kermany et al.16	108,312	CNV, DME, DRUSEN, H.E.	CLS	_	
Bogunovic et al.26	6,936	AMD, DME, RVO	SEG	IRF, SRF, PED	
Gholami ⁴²	470	AMD, DR, MH, CSR, H.E.	CLS	_	
Melinscak et al.43	1136	AMD	SEG	IRF, SRF, PED, Structure Layers	

Table 1. Overview of Publicly Accessible OCT Datasets Related to AMD or macular edema. **Note:** DME stands for Diabetes Retinal Edema, H.E. stands for Healthy Eye, RVO stands for Retinal Vein Occlusion, MH stands for Macula Hole, RPE stands for Retinal Pigment Epithelium, SEG stands for Segmentation, and CLS stands for Classification.

segmentation models leveraging characteristic AMD lesion features on OCT B-scan images^{17,18}, staging models^{19–21}, prognostic models^{22–25}. Notably, deep learning models demonstrate superior sensitivity and specificity in automated disease diagnosis, classification, and segmentation.

Table 1 presents publicly available OCT datasets related to AMD or macular edema. The Retouch dataset provides segmented images of edema that simultaneously include AMD, diabetic macular edema (DME), and retinal vein occlusion (RVO)²⁶. With a total of 6926 OCT B-scan images, it is currently the largest dataset for edema segmentation including IRF, SRF, and PED. However, wet AMD exhibits diverse pathological features on macular OCT slices, including but not limited to IRF, SRF, PED, SHRM, Ellipsoid zone (IS/OS) junction disruption, hyper-reflective dots, and vitreomacular adhesion. Studies by Simader C²⁷ and Waldstein SM²⁸ have shown a significant correlation between IRF, SRF, and PED with visual prognosis in wet AMD. Lai²⁹ further emphasized the importance of continuity in the Ellipsoid Zone, as its structural integrity also exhibits a strong correlation with visual prognosis. Research by Pokroy R³⁰ and Kumar JB³¹ focused on the impact of SHRM on visual prognosis in wet AMD, demonstrating its relevance as well.

Drawing inspiration from past research, the five pivotal features linked to visual decline and prognosis in wet AMD encompass IRF, SRF, PED, SHRM, and IS/OS junction disruption. Leveraging these insights, we manually annotated a high-quality OCT dataset containing five types of lesion labels by experienced ophthalmologists. Our dataset paves the way for creating various artificial intelligence-driven image segmentation models. This measure aims to intelligently simplify the evaluation of wet AMD and promote significant progress in clinical research.

Methods

Data collection. This study was approved by the Ethics Committee of The Second Affiliated Hospital of Nanchang University and adheres to the principles of the Helsinki Declaration (Approval Number: I-Medical Research Ethics Review [2023] No. 27). All patients included in the study were informed prior to their OCT examination that the images might be used for clinical research and released as public datasets. Informed consent was obtained from each patient. 3049 OCT B-scan images were collected from 138 patients (156 eyes) diagnosed with AMD from September 2023 to January 2024.

These patients were diagnosed and included in the dataset by three primary ophthalmologists (3-5 years of clinical experience) and one expert ophthalmologist (8 years of clinical experience) together. The exclusion criteria include (1) Patients with a history of vitrectomy surgery or the presence of intraocular filling substances in the vitreous cavity;(2) Patients with vitreoretinal diseases other than AMD, including but not limited to central serous chorioretinopathy, retinal artery occlusion, vein occlusion, macular hole, high myopic maculopathy, retinal detachment, diabetic retinopathy, retinitis pigmentosa, glaucoma, Coats' disease, optic nerve diseases, etc.;(3) Poor imaging quality, as defined by the following criteria: Signal strength of less than 5/10 on Cirrus HD-OCT 5000, partial horizontal B-scan missing, or structural incompleteness.

All patients underwent macular OCT scanning using the Zeiss Cirrus-HD-5000. These images were acquired by experienced ophthalmologists. During the scanning process, patients were in a seated position with their chin resting on a chin rest, and pupil dilation was performed when necessary. Patients were instructed to maintain a steady gaze to ensure that the scanning area was centered on the fovea. The majority of the OCT B-scans we selected were taken before any treatment, although there were also post-treatment images included. Given that we were engaged in the structural segmentation of OCT B-scan images from AMD patients, the amalgamation of additional features aids in a more comprehensive capture of clinical characteristics.

Image annotation. The OCT B-scan images segmentation annotation team consisted of three junior ophthalmologists and one expert ophthalmologist with over 8 years of experience. Initially, all images were annotated by the three junior ophthalmologists. Subsequently, the expert ophthalmologist reviewed and corrected all annotated images. Figure 1 illustrates the entire workflow of the segmentation annotation process. In the first step of the initial annotation (Fig. 1b), all three junior ophthalmologists manually outlined five anatomical structures (i.e., IRF, SRF, PED, SHRM, IS/OS) using the Labelme software.

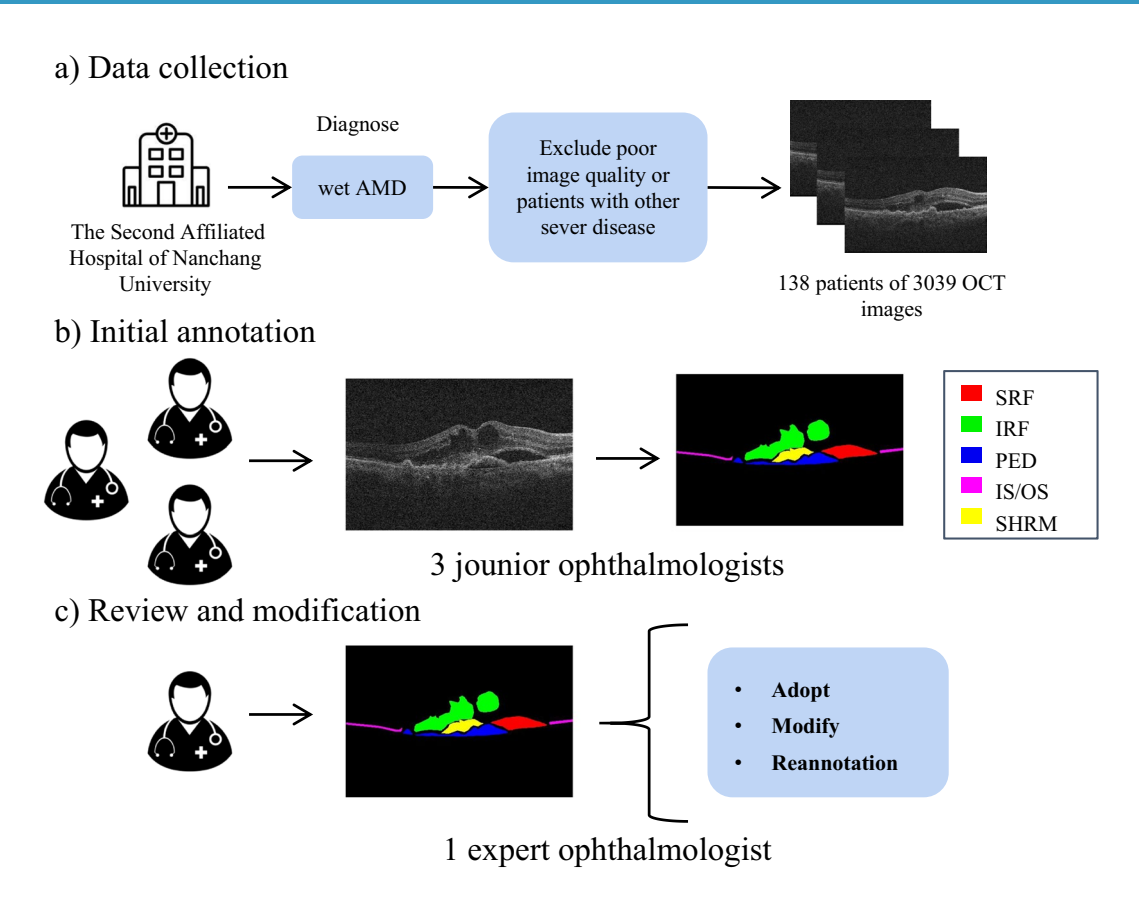


Fig. 1 The workflow for establishing the AMD-SD (a) Data collection. 138 patients were diagnosed with wet AMD at the Department of Ophthalmology of The Second Affiliated Hospital of Nanchang University. OCT B-scan was performed on 156 eyes of these patients, resulting in 3049 images. (b) Initial annotation. Three junior ophthalmologists manually annotated and segmented SRF, IRF, PED, SHRM, and IS/OS in OCT slices. (c) Review and modification. One expert ophthalmologist reviewed and validated all initial segmented images. Provide three types of evaluations, including adapt, modify, and reannotation, until all images pass expert review.

The annotation requirements are outlined as follows: (1) IRF: Refers to low-reflective exudates situated within the inner layers of the neurosensory retina. (2)SRF: Denotes low-reflective exudates located between the neurosensory retina and the retinal pigment epithelium (RPE). It is crucial to differentiate SRF from certain IRF near the RPE.(3)Ellipsoid zone (IS/OS): This represents a normal anatomical structure rich in mitochondria, demarcating the junction between the inner and outer segments of photoreceptors. It appears as a high-reflective signal band between the outer limiting membrane and the RPE layer. Annotation should proceed from left to right to ensure comprehensive coverage. In this study, we defined the annotation criteria as the outer limit of the myoid zone and the inner interface of the retinal pigment epithelium (Supplementary Fig. S1). When the Ellipsoid zone was damaged or could not be annotated due to image quality, the Ellipsoid zone annotation would be empty. The Ellipsoid zone was crucial in assessing retinal health, especially in AMD. Segmenting the Ellipsoid zone allows clinicians to precisely monitor changes over time, such as Ellipsoid zone disruption or thinning. (4) SHRM: Signifies high-reflective material situated between the retinal neuroepithelium and the RPE, possibly comprising various constituents such as exudates, fibrosis, blood, scars, or choroidal neovascularization. Careful differentiation from fibrovascular/hemorrhagic PED is necessary to prevent confusion, as some boundaries may be indistinct. (5)PED: This represents a characteristic feature of AMD, characterized by the separation of the RPE from the collagen within Bruch's membrane due to sub-RPE fluid accumulation. Initial identification of the RPE is essential for accurate annotation. In our study, PED was considered as the separation of the RPE from the collagen within Bruch's membrane due to sub-RPE fluid accumulation, including serous PED, vitelliform PED, and fibrovascular/hemorrhagic PED. For some small PEDs, it was sometimes difficult to distinguish them from drusenoid PEDs. If there was subretinal fluid or neovascular changes around them, we still considered them likely to be caused by sub-RPE fluid accumulation and annotated as PED.

In instances of poor-quality images, incomplete tissue morphology on OCT B-scans may occur due to noise or shadow artifacts. To minimize false-positive annotations and ensure segmentation accuracy, primary ophthalmologists should refrain from modifying image pixels, thereby preserving the original continuity of anatomical structures. We selected 20 to 60 B-scan slices containing representative and characteristic structures, and these selected images were nonconsecutive and distributed as widely as possible across the scope of the macular lesion. And we performed pixel-level annotation on specific structures. For some small lesions, we selected and annotated consecutive B-scan slices around the lesion, which might be fewer than 20 images. Those

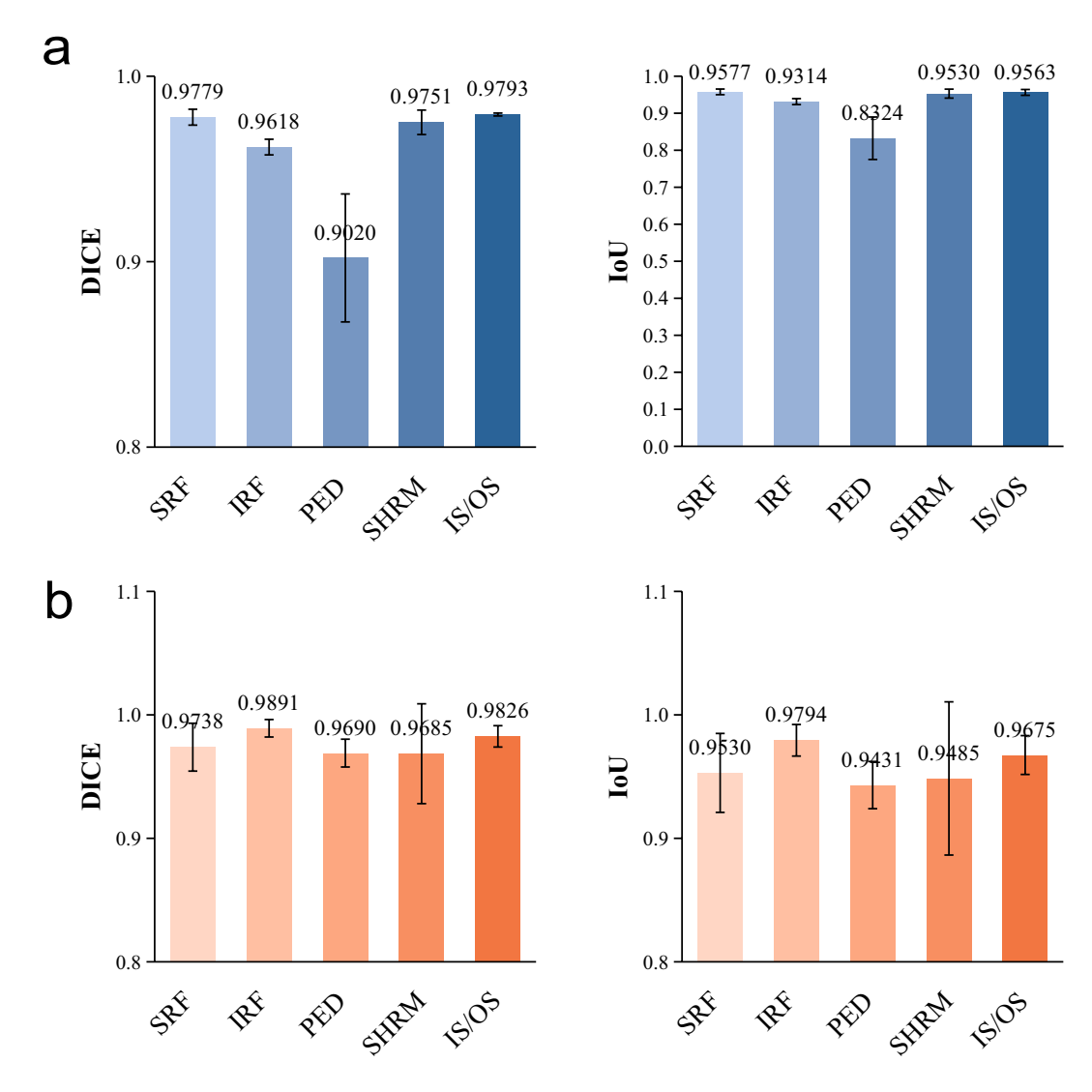


Fig. 2 The inter and intra segemation evaluation. (a) Inter-annotator agreement analysis. The average Dice coefficient was from 0.9020 to 0.9793. The average IoU was from 0.8324 to 0.9577. (b) Intra-annotator agreement analysis. The average Dice coefficient was from 0.9685 to 0.9891. The average IoU was from 0.9431 to 0.9794.

B-scans predominantly containing normal retinal tissue structures and needing few required annotations were not included.

The initial annotation images completed by all junior ophthalmologists were evaluated by the expert ophthalmologist, who then made corresponding decisions. The quality of the annotation was rated by the expert doctor in three categories: pass, modify, and reannotation. If all five labels were accurately annotated, no further modification was needed. If the rating was modified, the responsible junior doctor would need to make modifications under the guidance of the expert doctor. A small number of images rated as re-annotated would need to be re-annotated by the responsible junior ophthalmologist. During the annotation process, the expert ophthalmologist provided guidance and instructions to the junior ophthalmologists to improve the accuracy of the segmentation.

The inter-consistency and intra-consistency evaluation. To ensure consistent pixel-level image annotation among junior ophthalmologists, a structured approach was implemented. Initially, under the guidance of senior ophthalmologists, training sessions were conducted on annotation software usage and data annotation methodologies. Subsequently, three junior ophthalmologists were tasked with annotating the same set of 10 random B-scan slices from 10 different volumes to assess their understanding and consistency in identifying the five key structures in OCT B-scan images.

Following the basic annotation training, the average Intersection over Union (IoU) and Dice coefficients for SRF annotations by the three junior ophthalmologists were 0.9577 and 0.9779, respectively. Similarly, for IRF, the average IoU and Dice coefficients were 0.9314 and 0.9618, while for PED annotations, they were 0.8324 and 0.9020. SHRM annotations yielded average IoU and Dice coefficients of 0.9530 and 0.9751, and IS/OS labeling showed averages of 0.9563 and 0.9793. The evaluation of annotators' performance is presented in Fig. 2 and Supplementary Tables S1 and S2.

Item	Value	
Total number of participants	138	
Number of eyes	156	
Number of OCT B-scans	3,049	
Age, year (mean ± s.d.)	66.7 (9.1)	
Female (%)	61 (44.2%)	

Table 2. Data statistics of AMD-SD.

		Method					
Metrics	Type	U-Net ³³	U-Net++34	Att-UNet35	ResUNet ³⁶		
DICE	SRF	78.65	78.96	78.96	78.86		
	IRF	78.66	78.20	81.69	81.16		
	PED	79.62	77.37	79.61	81.88		
	SHRM	72.04	71.48	70.39	72.97		
	IS/OS	83.76	83.85	82.95	84.19		
	Mean	78.55	77.97	78.72	79.81		
IoU	SRF	64.81	65.24	65.23	65.11		
	IRF	64.82	64.21	69.05	68.33		
	PED	66.14	63.10	66.13	69.33		
	SHRM	56.37	55.62	54.30	57.44		
	IS/OS	72.06	72.19	70.86	72.70		
	Mean	64.48	64.07	65.11	66.58		

Table 3. Baseline image segmentation model results.

Moreover, to assess the intra-annotator consistency, three annotators independently performed pixel-level segmentation on the same 10 OCT B-scan images on different dates. The results are illustrated in Fig. 2b and Supplementary Tables S3 and S4. The average IoU and Dice coefficients for SRF were 0.9530 and 0.9738, for IRF they were 0.9794 and 0.9891, for PED annotations they were 0.9431 and 0.9690, for SHRM they were 0.9485 and 0.9685, and for IS/OS labeling, they were 0.9675 and 0.9826.

Although pixel-level annotation of most structures has achieved good consistency, significant deviations have been observed in the annotation of PED and SHRM according to Fig. 2 and Supplementary Tables. This is mainly because these two types of lesions have a relatively small proportion of pixels in the AMD dataset, and the annotators did not obtain sufficient consistency recognition in the initial stage of dataset establishment. The inter-consistency and intra-consistency evaluation identifies potential challenges in the annotation process, providing a foundation for improving the quality of collaborative annotation. All the final images were annotated after undergoing inter-consistency and intra-consistency evaluation, and all images were reviewed by the expert ophthalmologist.

Data Records

The AMD-SD is uploaded to the Figshare platform as a compressed file³². The extracted files are organized into one folder, one Microsoft Office Excel list, and two txt format files, named "Images" and "Demographics of the participants", "training" and "validation", respectively. In the "Images" folder, there are 156 sub-folders, each containing all images of an eye. Each image consists of two parts, with the original OCT B-scan image on the left and the expert segmentation mask on the right. The naming convention for images is "n_x.png", where "n" represents the eye ID and x represents the image number in a study. In the "Demographics of the participants" file, there are 5 columns. The first column represents the patient ID. The second column represents the eye ID. The third column represents the eye category. The fourth column represents the patient's age. The fifth column represents the patient's gender. The "training" and "validation" txt files store the specific image names for training and testing, respectively, following an 80:20 split of the dataset. The final OCT B-scan segmentation masks are six-color images, with red pixels representing SRF, pink pixels representing IS/OS, blue pixels representing PED, green pixels representing IRF, yellow pixels representing SHRM, and black pixels representing the background of the OCT.

The dataset consists of 3049 OCT B-scan images along with their corresponding lesion area segmentation masks. All images have a resolution of 570 x 380 pixels. The key features of the database are summarized in Table 2. These images are from 156 eyes of 138 patients, with 61 females and 77 males. The average age of the patients is 66.7 years with a standard deviation of 9.1 years. All participants are of Asian descent.

Technical Validation

To showcase the technical effectiveness of the dataset and offer insights into its statistical quality, we conducted supervised OCT B-scan image segmentation experiments. The objective of these experiments was to establish benchmark classification metrics that can serve as a reference for future research. We employed four fundamental and widely used image segmentation frameworks, namely U-Net³³, U-Net++³⁴, Att-UNet³⁵, and ResUNet³⁶. These methods have a strong track record in medical image segmentation tasks. We randomly divided the OCT

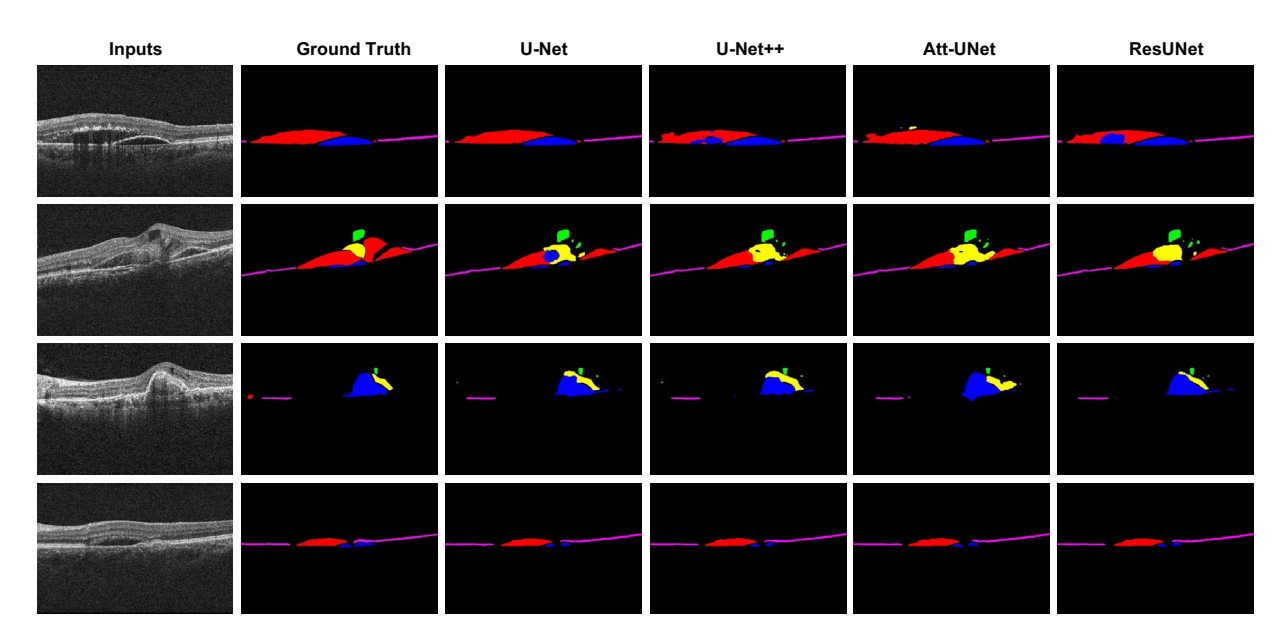


Fig. 3 Comparison of visual segmentation results. Red, blue, green, yellow, and pink colors represent SRF, PED, IRF, SHRM, and IS/OS, respectively.

examination studies into 80% for training and 20% for testing. The baseline segmentation performance of five distinct target areas was evaluated using the Dice Similarity Coefficient as the metric. The results of the OCT segmentation metrics for different structures are presented in Table 3. Figure 3 displays various input images in the test set, their doctor-annotated ground truth, and the results of different models. Additionally, the data partitioning used for training is included in our publicly available dataset.

The segmentation results demonstrate the capability of existing baseline segmentation models to converge with AI models on our dataset. This validates that existing models can generally learn from this dataset, reflecting a reliable segmentation. This further underscores the significance of our dataset in providing a foundational dataset for accurate assessment of wet AMD using OCT B-scan images.

Since our collected data all come from Cirrus-HD-5000, there may be potential performance differences on other brands of OCT devices. This is a limitation of our dataset that we must acknowledge. Furthermore, the current publicly available OCT dataset for AMD only covers IRF, SRF, and PED, while we provide additional SHRM and IS/OS segmentation, which will have a significant impact on this field. Our future work will focus on filling the gaps in the publicly available dataset regarding AMD evaluation features and achieving more precise assessments.

Usage Notes

The complete dataset is available for download via the provided link. Users have the flexibility to divide the dataset based on their specific study designs. It is expected that users will reference this paper in their research and recognize the dataset's contribution to their studies.

Code availability

The code mentioned in this study can be found at https://github.com/tsinghuamedgao20/Basic-Seg-Experiment.

Received: 3 April 2024; Accepted: 2 September 2024;

Published online: 18 September 2024

References

- 1. Wong, W. L. et al. Global prevalence of age-related macular degeneration and disease burden projection for 2020 and 2040: a systematic review and meta-analysis. *The Lancet Global Health* 2, e106–e116 (2014).
- 2. Colijn, J. M. *et al.* Prevalence of age-related macular degeneration in europe: the past and the future. *Ophthalmology* **124**, 1753–1763 (2017).
- 3. Eisenstein, M. Age-related macular degeneration (2021).
- 4. de Guimaraes, T. A. C., Varela, M. D., Georgiou, M. & Michaelides, M. Treatments for dry age-related macular degeneration: therapeutic avenues, clinical trials and future directions. *British Journal of Ophthalmology* 106, 297–304 (2022).
- 5. Guymer, R. H. & Campbell, T. G. Age-related macular degeneration. The Lancet (2023).
- Vottonen, P. Anti-vascular endothelial growth factors treatment of wet age-related macular degeneration: from neurophysiology to cost-effectiveness. Acta Ophthalmologica 96, 1–46 (2018).
- Chandra, S. et al. Ten-year outcomes of antivascular endothelial growth factor therapy in neovascular age-related macular degeneration. Eye 34, 1888–1896 (2020).
- 8. Hussain, R. M., Shaukat, B. A., Ciulla, L. M., Berrocal, A. M. & Sridhar, J. Vascular endothelial growth factor antagonists: promising players in the treatment of neovascular age-related macular degeneration. *Drug design, development and therapy* 2653–2665 (2021).

- 9. Cho, H. J. et al. Development of intraretinal fluid in neovascular age-related macular degeneration during anti-vascular endothelial growth factor treatment. American Journal of Ophthalmology 234, 6–14 (2022).
- 10. Kodjikian, L. et al. Early predictive factors of visual loss at 1 year in neovascular age-related macular degeneration under anti-vascular endothelial growth factor. Ophthalmology Retina 6, 109-115 (2022).
- 11. Bakri, S. J., Karcher, H., Andersen, S. & Souied, E. H. Anti-vascular endothelial growth factor treatment discontinuation and interval in neovascular age-related macular degeneration in the united states. *American Journal of Ophthalmology* **242**, 189–196 (2022)
- 12. MacCumber, M. W. et al. Antivascular endothelial growth factor agents for wet age-related macular degeneration: an iris registry analysis. Canadian Journal of Ophthalmology 58, 252–261 (2023).
- 13. Drexler, W. et al. Ultrahigh-resolution ophthalmic optical coherence tomography. Nature medicine 7, 502-507 (2001).
- 14. Fujimoto, J. G. Optical coherence tomography for ultrahigh resolution in vivo imaging. Nature biotechnology 21, 1361-1367 (2003).
- 15. Treder, M., Lauermann, J. L. & Eter, N. Automated detection of exudative age-related macular degeneration in spectral domain optical coherence tomography using deep learning. *Graefe's Archive for Clinical and Experimental Ophthalmology* **256**, 259–265 (2018).
- 16. Kermany, D. S. et al. Identifying medical diagnoses and treatable diseases by image-based deep learning. cell 172, 1122–1131 (2018).
- 17. Moraes, G. *et al.* Quantitative analysis of oct for neovascular age-related macular degeneration using deep learning. *Ophthalmology* **128**, 693–705 (2021).
- 18. Xie, H., Xu, W., Wang, Y. X. & Wu, X. Deep learning network with differentiable dynamic programming for retina oct surface segmentation. *Biomedical optics express* 14, 3190–3202 (2023).
- Seeböck, P. et al. Unsupervised identification of disease marker candidates in retinal oct imaging data. IEEE transactions on medical imaging 38, 1037–1047 (2018).
- Motozawa, N. et al. Optical coherence tomography-based deep-learning models for classifying normal and age-related macular degeneration and exudative and non-exudative age-related macular degeneration changes. Ophthalmology and therapy 8, 527–539 (2019).
- 21. Rim, T. H. *et al.* Detection of features associated with neovascular age-related macular degeneration in ethnically distinct data sets by an optical coherence tomography: trained deep learning algorithm. *British Journal of Ophthalmology* **105**, 1133–1139 (2021).
- 22. Schmidt-Erfurth, U. et al. Prediction of individual disease conversion in early amd using artificial intelligence. Investigative ophthalmology & visual science 59, 3199-3208 (2018).
- 23. Yim, J. et al. Predicting conversion to wet age-related macular degeneration using deep learning. Nature Medicine 26, 892–899 (2020).
- 24. Romo-Bucheli, D., Erfurth, U. S. & Bogunović, H. End-to-end deep learning model for predicting treatment requirements in neovascular amd from longitudinal retinal oct imaging. *IEEE Journal of Biomedical and Health Informatics* 24, 3456–3465 (2020).
- Bogunović, H., Mares, V., Reiter, G. S. & Schmidt-Erfurth, U. Predicting treat-and-extend outcomes and treatment intervals in neovascular age-related macular degeneration from retinal optical coherence tomography using artificial intelligence. Frontiers in Medicine 9, 958469 (2022).
- Bogunović, H. et al. Retouch: The retinal oct fluid detection and segmentation benchmark and challenge. IEEE transactions on medical imaging 38, 1858–1874 (2019).
- 27. Simader, C. et al. Morphologic parameters relevant for visual outcome during anti-angiogenic therapy of neovascular age-related macular degeneration. *Ophthalmology* 121, 1237–1245 (2014).
- 28. Waldstein, S. M. et al. Predictive value of retinal morphology for visual acuity outcomes of different ranibizumab treatment regimens for neovascular amd. Ophthalmology 123, 60–69 (2016).
- 29. Lai, T.-T., Hsieh, Y.-T., Yang, C.-M., Ho, T.-C. & Yang, C.-H. Biomarkers of optical coherence tomography in evaluating the treatment outcomes of neovascular age-related macular degeneration: a real-world study. *Scientific Reports* 9, 529 (2019).
- 30. Pokroy, R. et al. Prognostic value of subretinal hyperreflective material in neovascular age-related macular degeneration treated with bevacizumab. Retina 38, 1485–1491 (2018).
- 31. Kumar, J. B., Stinnett, S., Han, J. I. & Jaffe, G. J. Correlation of subretinal hyperreflective material morphology and visual acuity in neovascular age-related macular degeneration. *Retina* 40, 845–856 (2020).
- 32. Author, T. Amd-sd: An optical coherence tomography image dataset for wet amd lesions segmentation. *Figshare* https://doi.org/10.6084/m9.figshare.c.7157554.v1 (2024).
- 33. Ronneberger, O., Fischer, P. & Brox, T. U-net: Convolutional networks for biomedical image segmentation. In *Medical Image Computing and Computer-Assisted Intervention–MICCAI 2015: 18th International Conference, Munich, Germany, October 5-9, 2015, Proceedings, Part III 18, 234–241* (Springer, 2015).
- 34. Zhou, Z., Siddiquee, M. M. R., Tajbakhsh, N. & Liang, J. Unet++: Redesigning skip connections to exploit multiscale features in image segmentation. *IEEE transactions on medical imaging* 39, 1856–1867 (2019).
- 35. Oktay, O., *et al.* Attention u-net: Learning where to look for the pancreas. *arXiv preprint arXiv:1804.03999* (2018).
- 36. Zhang, Z., Liu, Q. & Wang, Y. Road extraction by deep residual u-net. IEEE Geoscience and Remote Sensing Letters PP, 1-5 (2017).
- 37. Chiu, S. J. et al. Validated automatic segmentation of amd pathology including drusen and geographic atrophy in sd-oct images. Investigative ophthalmology & visual science 53, 53–61 (2012).
- 38. Farsiu, S. *et al.* Quantitative classification of eyes with and without intermediate age-related macular degeneration using optical coherence tomography. *Ophthalmology* **121**, 162–172 (2014).
- 39. Srinivasan, P. P. et al. Fully automated detection of diabetic macular edema and dry age-related macular degeneration from optical coherence tomography images. *Biomedical optics express* 5, 3568–3577 (2014).
- 40. Chiu, S. J. et al. Kernel regression based segmentation of optical coherence tomography images with diabetic macular edema. Biomedical optics express 6, 1172–1194 (2015).
- 41. Rashno, A. et al. Fully-automated segmentation of fluid regions in exudative age-related macular degeneration subjects: Kernel graph cut in neutrosophic domain. *PloS one* 12, e0186949 (2017).
- 42. Gholami, P., Roy, P., Parthasarathy, M. K. & Lakshminarayanan, V. Octid: Optical coherence tomography image database. *Computers & Electrical Engineering* 81, 106532 (2020).
- 43. Melinščak, M., Radmilović, M., Vatavuk, Z. & Lončarić, S. Annotated retinal optical coherence tomography images (aroi) database for joint retinal layer and fluid segmentation. *Automatika: časopis za automatiku, mjerenje, elektroniku, računarstvo i komunikacije* 62, 375–385 (2021).

Acknowledgements

This work was supported by grants from the National Natural Science Foundation of China (82360204; 82160203); the Natural Science Foundation Youth Fund Project Of Jiangxi Province (20224BAB216049); and the Science and Technology project of Jiangxi Administration of Traditional Chinese Medicine (2023B0368). National Natural Science Foundation incubation project of The Second Affiliated Hospital of Nanchang University (2022YNFY12004). The authors report there are no competing interests to declare.

Author contributions

Y.H., Y.G., and W.G. were responsible for the conceptualization and design of the study. Y.H., Y.G., W.L., and Z.Y. were responsible for data annotation. F.X., Z.C., Y.L., and X.X. contributed to data collection and assisted in manuscript writing. Y.H., W.G., and L.M. participated in the technical validation. X.Y., X.D., L.M., and G.L. collectively supervised this research's progress. All authors contributed to the article and approved the submitted version.

Competing interests

The authors declare no competing interests.

Additional information

Supplementary information The online version contains supplementary material available at https://doi. org/10.1038/s41597-024-03844-6.

Correspondence and requests for materials should be addressed to X.Y., Y.D., L.M. or G.L.

Reprints and permissions information is available at www.nature.com/reprints.

Publisher's note Springer Nature remains neutral with regard to jurisdictional claims in published maps and institutional affiliations.

Open Access This article is licensed under a Creative Commons Attribution-NonCommercial-NoDerivatives 4.0 International License, which permits any non-commercial use, sharing, distribution and reproduction in any medium or format, as long as you give appropriate credit to the original author(s) and the source, provide a link to the Creative Commons licence, and indicate if you modified the licensed material. You do not have permission under this licence to share adapted material derived from this article or parts of it. The images or other third party material in this article are included in the article's Creative Commons licence, unless indicated otherwise in a credit line to the material. If material is not included in the article's Creative Commons licence and your intended use is not permitted by statutory regulation or exceeds the permitted use, you will need to obtain permission directly from the copyright holder. To view a copy of this licence, visit http://creativecommons.org/licenses/by-nc-nd/4.0/.

© The Author(s) 2024